



RESEARCH ARTICLE

The oscillating vortex generator: a boundary layer propulsion and flow control device

B. Anilir¹, D.F. Kurtulus¹ and M.F. Platzer²

¹Aerospace Engineering Department, Middle East Technical University, Ankara, Turkey

²University of California, Davis, Davis, CA, USA

Corresponding author: B. Anilir; Email: anilir.berkan@metu.edu.tr

Received: 4 March 2024; **Revised:** 1 August 2024; **Accepted:** 6 August 2024

Keywords: plunging airfoil; ground effect; micro air vehicle

Abstract

This paper aims to explore the feasibility of providing boundary layer propulsion and flow control by means of embedded aerofoils that are oscillating in the pure plunge mode. To this end, Navier-Stokes calculations of the low-speed flow over a flat plate with an oscillating small foil in close vicinity to the plate were performed to determine the influence of the wall distance, Reynolds number, and reduced frequency on the aerofoil thrust. The simulations were extensively validated against water tunnel experiments at Reynolds numbers between 440 to 5,940. Good agreement was obtained in terms of mean streamwise velocity profiles and the vortical wake patterns. Results indicate that the thrust increases from its value in unbounded flow with decreasing distance from the plate. The propulsive efficiency exhibits a consistent peak at a non-dimensional plunge velocity of about 0.55. For wall distances between one-half to one chord lengths, vortex pairs are shed in a slightly upward deflected direction independent of the starting motion of the aerofoil. As the wall distance increases further, these vortex pairs change into the well-known reverse Karman vortex street. Example calculations for a flat plate with two foils mounted close to the plate trailing edge and oscillating in counterphase confirm the device's efficacy.

Nomenclature

c	chord length
C_t	thrust coefficient
C_p	power coefficient
dy	wall distance
f	plunge frequency
h	plunge position
h_0	plunge amplitude
k	reduced frequency, $= \omega c / U_\infty$
Re	Reynolds number, $\rho U_\infty c / \mu$
Re_θ	momentum thickness Reynolds number
U_∞	freestream velocity
v_p	non-dimensional plunge velocity, $= k(h_0/c)$
ITA	iterative time advancement scheme
MAV	micro-air-vehicle
OVG	oscillating vortex generators
PISO	pressure-implicit with splitting of operator
SST	shear-stress transport
URANS	unsteady Reynolds-averaged Navier-Stokes
VG	vortex generators

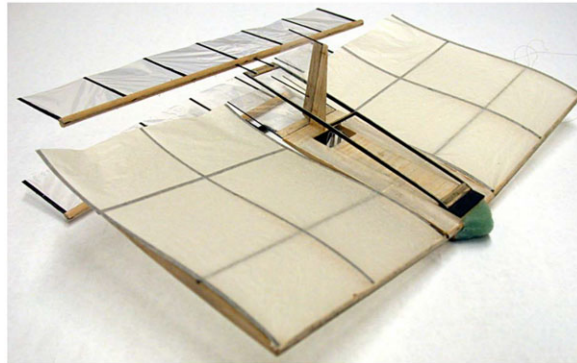


Figure 1. Micro air vehicle with two wings flapping in counterphase [1].

γ	intermittency
η	propulsive efficiency, $= C_i/C_p$
ρ	fluid density
ω	angular frequency, $= 2\pi f$

1.0 Introduction

The flapping wing micro air vehicle shown in Fig. 1 is propelled by means of two biplane high aspect ratio wings that are flapping with a 180 degree phase angle in both pitch and plunge. The biplane arrangement enables the exploitation of the ground effect. The aerodynamic phenomenon of lift increase on an aerofoil due to flight near the ground [1] seems to have been first noticed in flights of the Dornier DO-X seaplane where its payload and range could be increased by flying near the water during its transatlantic flight in the early 1930s. Since then, it sparked interest in building various wing-in-ground effect vehicles, culminating in the Russian Caspian Sea Monster ekranoplan. It is much less appreciated that flight in ground effect also increases the thrust due to wing flapping near the ocean surface, enabling albatrosses to minimise energy for their long-distance flights. It found a technical application only recently in the development of the micro-air-vehicle (MAV) shown in Fig. 1. The two wings are forced to oscillate in counterphase, thus reproducing the effect of a single wing oscillating near a ground plane. The numerical and experimental investigations that were conducted prior to the flight of this MAV in 2002 are reported in references [1,2]. Other studies of the aerodynamics of oscillating aerofoils in ground effect are those of Moryossef and Levy [3], Liang et al. [4], Molina and Zhang [5], Wu et al. [6], Sarbandi et al. [7], and Rozhdestvensky [8].

A second important feature implemented in the design of the MAV of Fig. 1 is the placement of the two flapping wings close to the trailing edge of the stationary main wing. This arrangement allows the flapping wings to serve as both propulsion and flow control device because the flapping wings function as two-dimensional propellers drawing air over the stationary wing into the propellers. This makes it possible to delay the wing stall of the stationary wing to angles of attack of about 30 degrees, as was observed in the MAV flight tests.

The explanation of thrust generation by means of flapping wings dates back to Knoller [9] and Betz [10]. The Knoller-Betz effect was experimentally confirmed by Katzmayer [11] by placing a stationary aerofoil into an oscillatory wind stream. In either case, a stationary aerofoil in an oscillatory flow or an oscillating aerofoil in a uniform flow, the aerofoil experiences a thrust force, and a vortex wake is shed from the trailing edge that is the exact opposite of the Karman vortex street. Measurements of the time-averaged velocity profiles generated by such reverse Karman vortex streets reveal them to be jet profiles, thus confirming that oscillating aerofoils can be regarded as small jet engines. By now, the aerodynamics of flapping wings is well understood and documented, for example by Shyy et al. [12].

It is important to be aware of the fact that the efficacy of flapping wing propulsion is critically dependent on the magnitude of the Strouhal number at which the wings are flapping. Since the frequency and amplitude of the flapping wings are in the numerator and the flight speed is in the denominator, the Strouhal number necessary for efficient flight cannot easily be maintained because of the limitations on flapping frequency and amplitude. As a consequence, the general view is that flapping wing vehicles are likely to be confined to low flight speeds and small sizes. The question arises whether flapping aerofoils may still be useful in achieving boundary layer control and even boundary layer propulsion on conventional aerofoils [13].

As already mentioned, the efficacy of flapping wings depends on operating in very low speed flows. This suggests using them to reduce separated flow regions. Indeed, Lai et al. [14] measured drastic reductions of the separated flow region behind a backward-facing step by oscillating a small foil in the separation region. Dohring [15] visualised the flow over a profile with an S-shaped trailing edge, as shown in Fig. 5 of Ref. [1] or over a profile with a rounded trailing edge and observed the elimination of the separated flow regions by oscillating a small aerofoil close to the profiles' trailing edges. The present authors [16] examined this flow by means of a Navier-Stokes analysis and found that the oscillating foil changes the separated flow into a well-organised vortex street.

These findings suggest to eliminate separated flow regions on conventional airplane wings. The flow near the trailing edge of such wings typically exhibits a small separated flow region. Its presence requires to account for the resulting pressure drag contribution to the total profile drag by means of the Squire-Young formula. Therefore, it stands to reason that the placement of small flapping aerofoils in the very low flow region near the trailing edge of high Reynolds number wings may produce a beneficial drag reduction effect or even a small boundary layer propulsion effect.

For this reason, the exploration of the aerodynamic characteristics of oscillating aerofoils close to an aerofoil surface may be promising for the purpose of assessing their potential for boundary layer energisation. A number of basic flow studies need to be completed before attempting to apply it to aerofoils at large Reynolds numbers. The most economical way to proceed is to conduct computational studies at increasing Reynolds numbers before selecting experiments to confirm the predictions. Therefore, in this paper the low-speed flow over a small aerofoil that executes plunging oscillations near a flat plate boundary layer is analysed computationally at low Reynolds numbers to determine the effect of wall distance and reduced frequency and to validate the code with the LDV flow measurements obtained by Dohring [15].

2.0 Computational setup

Dohring [15] used a 760mm long flat plate aligned with the water flow and a NACA 0012 aerofoil of 20mm chord length c whose leading edge was located 100mm downstream of the plate leading edge, Fig. 2(a). The computations are performed as the aerofoil undergoes a periodic plunging motion given by Equation (1) The geometric angle-of-attack of the aerofoil is set to 0° . The distance between the flat plate and the plunging NACA0012 aerofoil is called the wall distance (dy). It ranges between $0.4c$ to $1.5c$, corresponding to 8 to 30mm. The plunging amplitude h of the aerofoil is $0.088c$, corresponding to 1.76mm.

Figure 2(b) shows the schematic diagram of counter-rotating biplane aerofoil near the flat plate. This configuration is built to illustrate the MAV shown in Fig. 1. The two aerofoils are again flapping in counterphase, but they are mounted upstream of the plate trailing edge. The aerofoil distance from the plate was varied up to a distance where the foils were flapping outside of the plate boundary layer. The flat plate has semi-circular rounded leading and trailing edges, and its thickness and length are set to $0.5c$ and $5c$, respectively.

The sinusoidal plunging position (h) of the aerofoil and the angular frequency (ω) are defined by Equations (1) and (2), respectively.

$$h(t) = h_0 \sin(\omega t) \quad (1)$$

$$\omega = 2\pi f \quad (2)$$

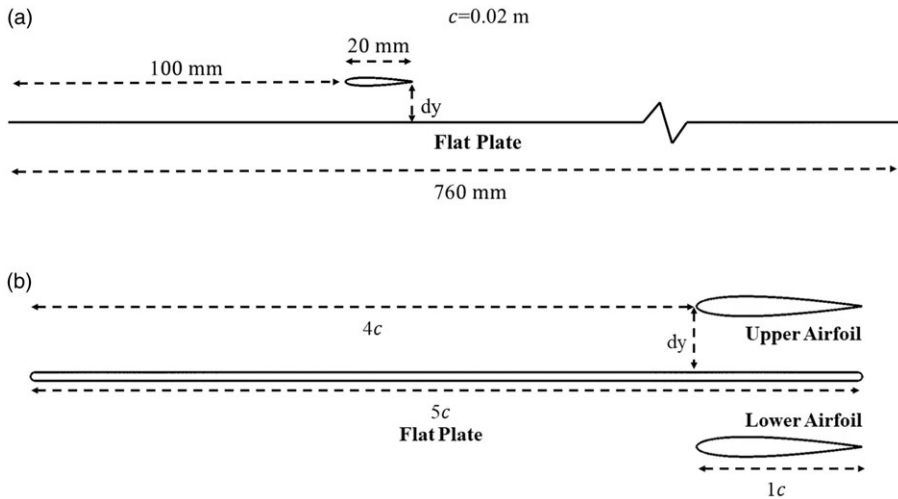


Figure 2. Schematic diagram of (a) single plunging aerofoil near the flat plate and (b) counter-plunging biplane aerofoil near the flat plate.

where h_0 is the plunge amplitude, and f is the plunge frequency in Hz. Other critical parameters for the plunge motion are the reduced frequency (k) (Equation 3) and non-dimensional plunge velocity (v_p) (Equation 4).

$$k = \omega c / U_\infty \tag{3}$$

$$v_p = k (h_0 / c) \tag{4}$$

where c is the chord length, and U_∞ the freestream velocity. The propulsive efficiency (η) is then defined by the ratio between the mean thrust (C_t) and mean power (C_p) coefficients.

$$\eta = C_t / C_p \tag{5}$$

The mean power coefficient is computed by integrating the lift coefficient times the plunge velocity on the plunging aerofoil, as shown in Equation (6). Time-averaged data is obtained by taking the mean of 10 complete oscillations after periodic conditions are reached.

$$C_p = \frac{1}{\Delta t} \int_{\Delta t} (c_l \dot{h} / U_\infty) dt \tag{6}$$

3.0 Numerical method

The two-dimensional low-Reynolds-number incompressible flow over the plunging NACA0012 near the flat plate is simulated numerically with a commercial finite volume solver of ANSYS Fluent v17.2 [17] by solving the unsteady Reynolds-averaged Navier-Stokes (URANS) equations. The numerical solution is obtained by evaluating the gradients using the Least Squares Cells-Based scheme. The second-order upwind scheme was adopted as the method to discretise pressure, momentum, turbulent kinetic energy, specific dissipation rate, intermittency and momentum thickness Re equations. The transient formulation uses the second-order implicit iterative time advancement scheme (ITA). The advantage of the implicit scheme is that it is unconditionally stable with respect to time-step size [17]. Pressure-velocity coupling is done by a segregated type algorithm of PISO (pressure-implicit with splitting of operators) and the details of the algorithm can be found in Ferziger et al. [18]. For the pure plunging simulations of a single NACA0012 aerofoil, the motion of the aerofoil is introduced by rigid-body motion of the whole

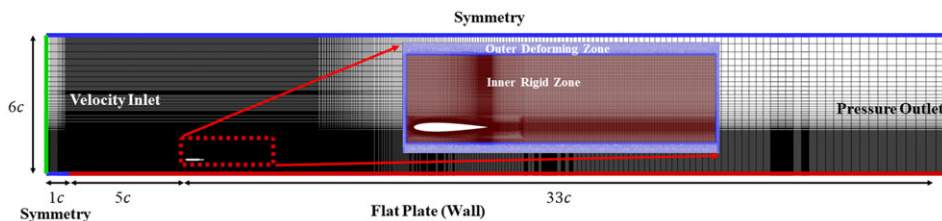


Figure 3. Computational domain.

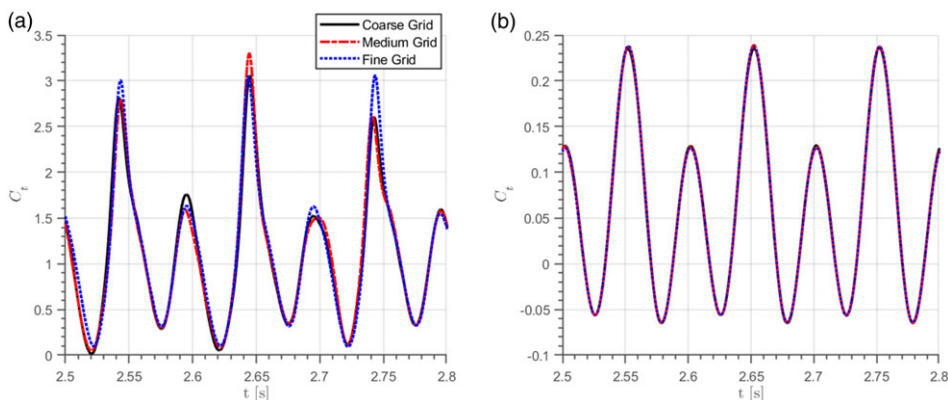


Figure 4. Time history of the thrust coefficient at (a) $Re = 1,960$, $k = 12.7$, $dy = 0.4c$ and (b) $Re = 5,940$, $k = 4.2$, $dy = 0.4c$.

domain. The high-quality structured grid near the NACA0012 aerofoil (shown in Fig. 3 as red region named inner rigid zone) moves together with the aerofoil as a rigid body, and the blue-coloured region is a deformable grid. Other regions coloured as grey are set as stationary and non-deformable (see Fig. 2).

The numerical simulations were conducted with the transitional turbulence model of the shear-stress transport (SST) γ - Re_θ model (also known as Transition SST model), which couples the k - ω SST model of Menter [19] with two transport equations for intermittency (γ) and momentum thickness Reynolds number (Re_θ) (Langtry and Menter [20]). The model has been used and validated at low Reynolds number external flow over an aerofoil in the literature by Counsil and Boulama [21], Chen et al. [22] and Ruiz and D'Ambrosio [23]. Time-averaged (mean) data is obtained by taking the mean of a sufficiently large number of complete oscillations after periodic conditions are reached.

The velocity inlet is placed sufficiently far upstream to ensure uniform freestream flow at the beginning of the flat plate. The inlet is $1c$ upstream of the leading edge of the flat plate. The bold blue lines at the top and bottom boundaries show the symmetry boundary conditions. Also, the bold red line (total $38c$ length) at the bottom boundary indicates the flat plate with wall boundary condition.

3.1 Grid refinement study

In our previous papers [16,24], the grid refinement study was carried out by adjusting the number of points around a plunging NACA0012 aerofoil and the structured cells at the near wake. Therefore, the inner rigid zone (red region) shown in the Fig. 3 is the same as in the previous studies and the number of points around the aerofoil surface is equal to 760. For this study, the grid refinement was only applied to the cell on the flat plate surface at $Re = 1,960$, $k = 12.7$, $dy = 0.4c$, and $Re = 5940$, $k = 4.2$, $dy = 0.4c$. Three different grids, named as coarse, medium and fine grids, were employed with a refinement ratio of around 1.5. The time history of the plunging aerofoil's thrust coefficient is presented in Fig. 4. It is

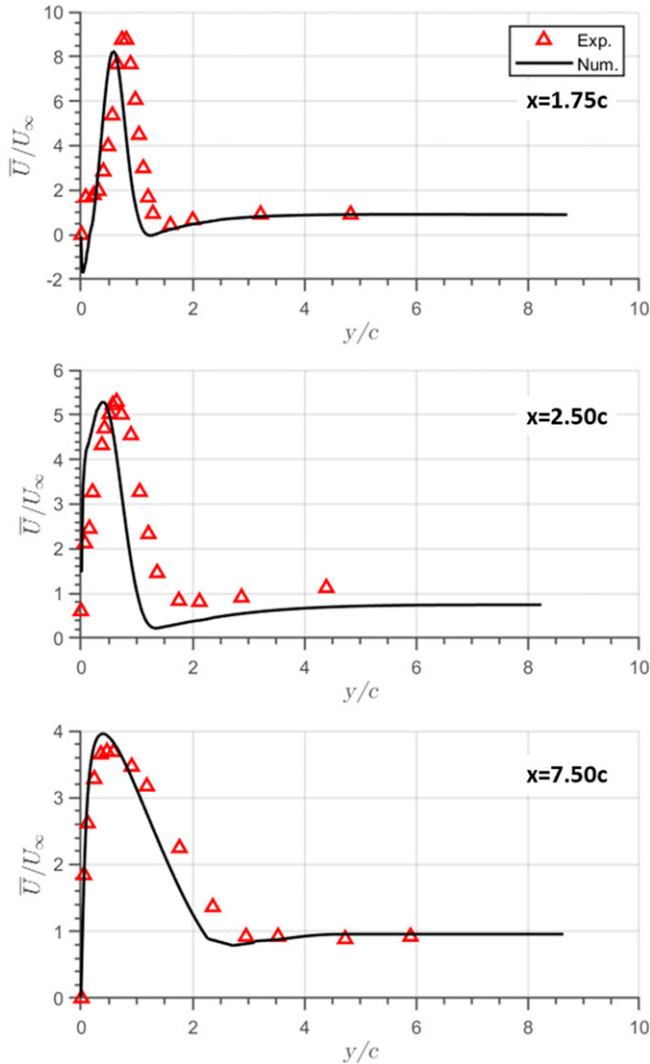


Figure 5. Comparison of the mean streamwise velocity profiles at three wake distances for $k = 57$, $v_p = 5.03$, $Re = 440$, $dy = 0.4c$.

found that the medium grid is sufficiently refined and the results are very close to the fine grid. The step size of 0.0002s (500 time steps within a plunge cycle) based on the previous time refinement studies is selected.

4.0 Validation of the numerical simulations

The numerical simulations are validated against the published experimental results of Dohring [15] at several reduced frequencies, Reynolds numbers and wall distances. The experiments were carried out in a water tunnel by conducting Laser Doppler measurements and flow visualisation for the case of a plunging aerofoil in close proximity to a flat plate. Figure 5 shows the comparison between the computed and measured velocity distributions at three different measuring stations downstream of the foil trailing edge for a freestream velocity of 0.022m/s, corresponding to a Reynolds number of 440 based

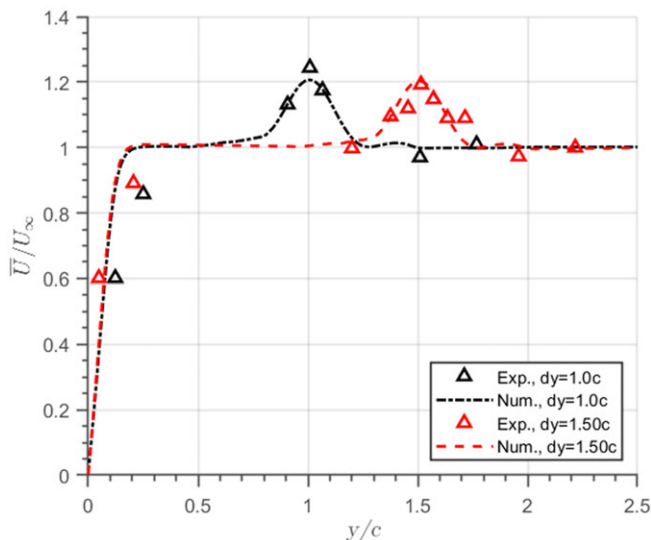


Figure 6. Comparison of the mean streamwise velocity profiles at the wall distances $dy = 1.0$ and $dy = 1.5$ for $k = 4.2$, $v_p = 0.37$, $Re = 5,940$.

on the foil chord. The laminar flat plate boundary layer thickness at the foil leading edge (located 100mm downstream from the leading edge of the flat plate) then is 10mm. The foil distance from the flat plate, the wall distance dy , is 8.5mm, corresponding to a non-dimensional wall distance $dy = 0.425c$. The aerofoil is therefore just barely immersed in the boundary layer. The amplitude of oscillation is 1.76mm and the frequency of 10Hz corresponds to a reduced frequency of 57. The time-averaged velocity profiles downstream of the aerofoil trailing edge are shown at distances 135, 150 and 200mm from the plate leading edge, corresponding to local boundary layer thicknesses of 12.4, 13 and 16.9mm, respectively. The formation of a jet profile is clearly seen, decreasing from a value of more than eight times the freestream velocity at a distance of 1.75c to four times at a distance of 7.5c. These profiles are predicted quite well. At large downstream distances the jet has dissipated into the freestream.

In Fig. 6, the comparisons are shown for two much larger wall distances $dy = 1.0c$ and $1.5c$, corresponding to distances of 20 and 30mm, respectively. Consequently, the aerofoil is outside of the boundary layer. The free-stream speed is 3m/s corresponding to a Reynolds number of 5,940, the frequency is 10Hz corresponding to a reduced frequency $k = 4.2$. As expected, the jet profiles are much smaller than in Fig. 5. The agreement between experiment and computation is quite good.

Similarly, the velocity profiles are shown in Fig. 7 for the wall distances of $dy = 0.4c$ and $1.25c$, corresponding to distances of 8 and 25mm, respectively. The free stream speed is 0.1m/s corresponding to a Reynolds number of 1960 and the frequency is 10Hz corresponding to a reduced frequency of 12.7. It is seen that the maximum velocity is larger at the larger wall distance compared to the maximum velocity at the much smaller wall distance. This indicates that there exists a maximum velocity for different parameter combinations of wall distance and plunge velocity. A comparison of the optimal wall distances obtained from the measurements and computations is given in Table 1. It is seen that the optimal distance increases with increasing plunge velocity. The comparison is shown in Fig 8 for four plunge velocities. It is quite good with the exception of a few points in Fig. 8(b), (c) and (d) that require further investigation.

Furthermore, it is also interesting to note the upstream effect in front of the foil leading edge, shown in Fig. 9 At the two distances $0.4c$ and $0.75c$ in front of the leading edge, corresponding to 8 and 15mm, the flow speed increases in both the experiment and computation. The differences are attributable to the measuring inaccuracy.

Table 1. Optimal wall distances

k	v_p	Optimal dy (Dohring [15])	Optimal dy (Num.)
4.2	0.37	0.65c	0.40c
6.3	0.55	0.90c	0.50c
8.4	0.74	1.50c	0.60c
12.7	1.21	1.25c	0.90c

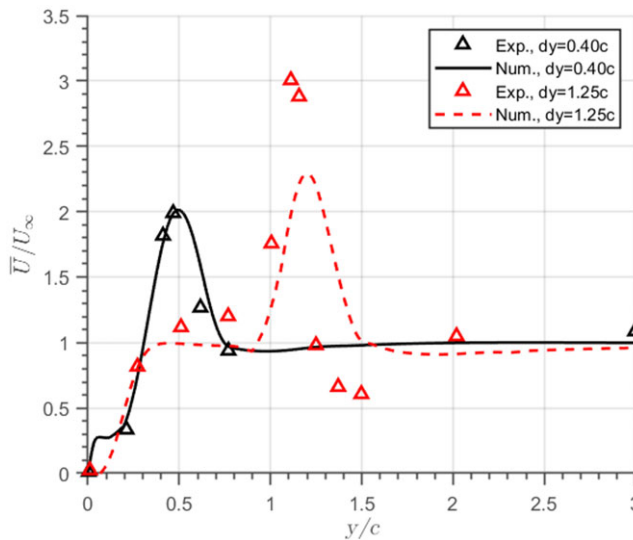


Figure 7. Comparison of the mean streamwise velocity profiles at the wall distances $dy = 0.4c$ and $1.25c$ for $k = 12.7$, $v_p = 1.12$, $Re = 1,960$.

Finally, Fig. 10 shows the comparison between Dohring’s flow visualisation of the vortical wakes shed from the trailing edge of the plunging foil for a plunge velocity of 0.37 at the two wall distances $dy = 0.6c$ and $1.1c$. The agreement is quite good. At the closer distance the vortical wake is deflected upward from the wall. At the larger distance the vortical wake remains symmetrical in agreement with the expected behaviour in unbounded flow at this plunge velocity.

5.0 Computational prediction of the aerodynamic characteristics of plunging naca 0012 profiles as a function of wall proximity

For the application of small oscillating aerofoils to boundary layer propulsion, it is necessary to know their thrust, lift and efficiency. In this section the above described URANS simulations are used to predict the aerodynamic characteristics of NACA 0012 profiles oscillating in the pure plunge mode at various distances from the wall. Figure 11 shows the variation of the thrust and lift coefficients and of the propulsive efficiency for wall distances between $0.5c$ to $5.0c$ at various plunge velocities and Reynolds numbers. The dashed line indicates the values for the foil in unbounded flow. It is seen that the thrust force produced by the plunging aerofoil near the flat plate is always greater than that of the single plunging aerofoil in unbounded flow, but continuously decreases with increasing distance to approach the unbounded flow value. A similar behaviour is observed for the lift and the propulsive efficiency. As expected, the thrust increases with increasing plunge velocity, whereas the propulsive efficiency exhibits a consistent peak at a plunge velocity of about 0.55, as shown in Fig. 12.

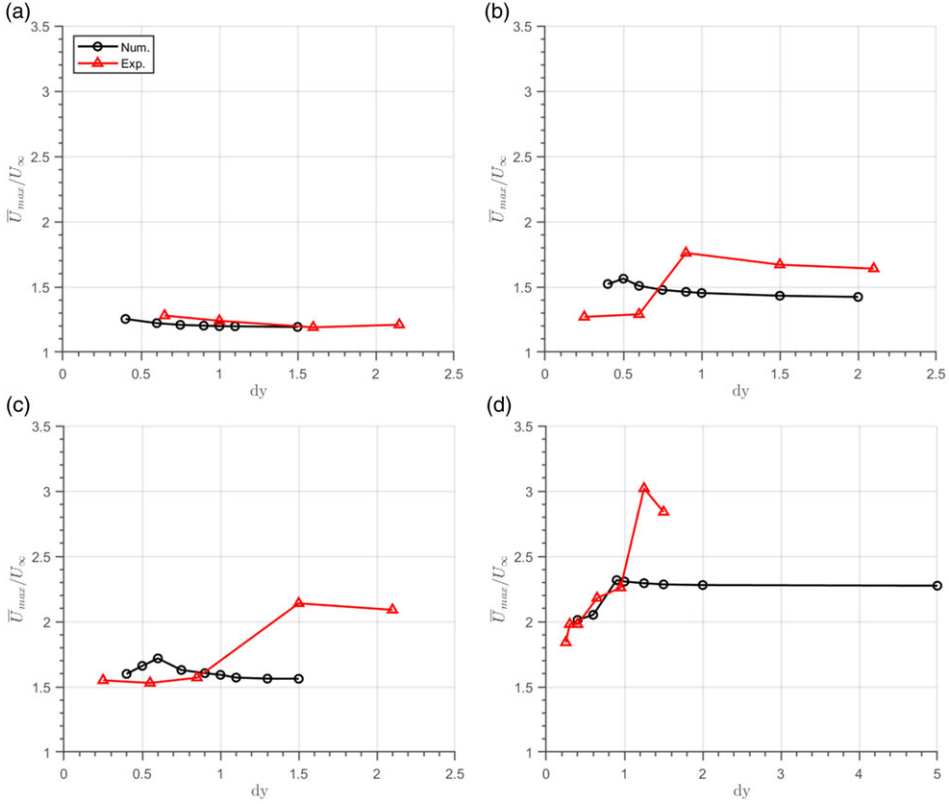


Figure 8. Variation of the nondimensional maximum velocity in the velocity profiles obtained at $x = 1.75c$ at (a) $k = 4.2$, (b) $k = 6.3$, (c) $k = 8.4$, and (d) $k = 12.7$.

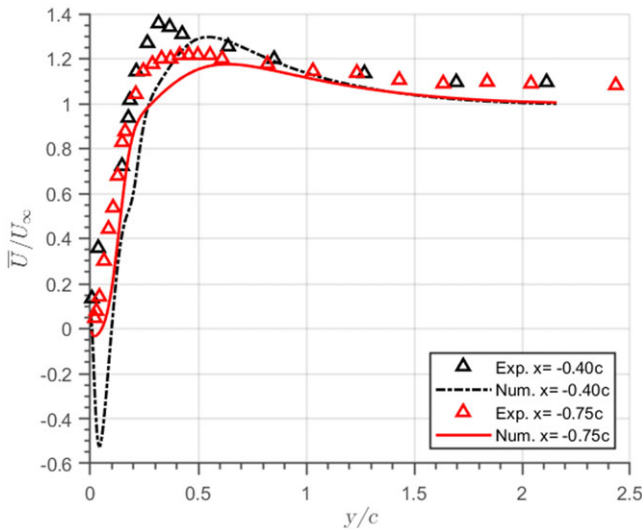


Figure 9. Comparison of measured and computed velocity profiles upstream of the foil leading edge for $k = 57$, $dy = 0.6c$.

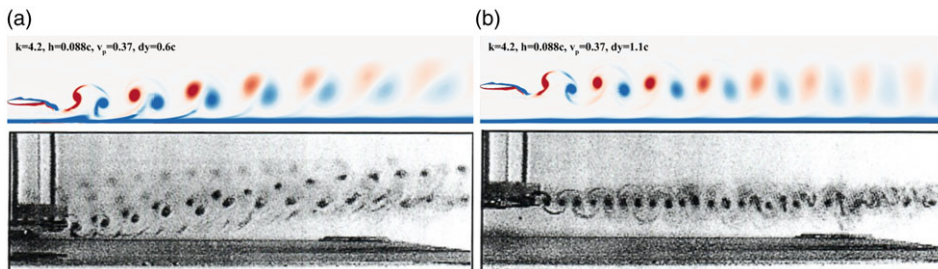


Figure 10. Comparison of vortical patterns between numerical simulations and Dohring's water tunnel experiments $v_p = 0.37$, (a) $dy = 0.6c$, and (b) $dy = 1.1c$.

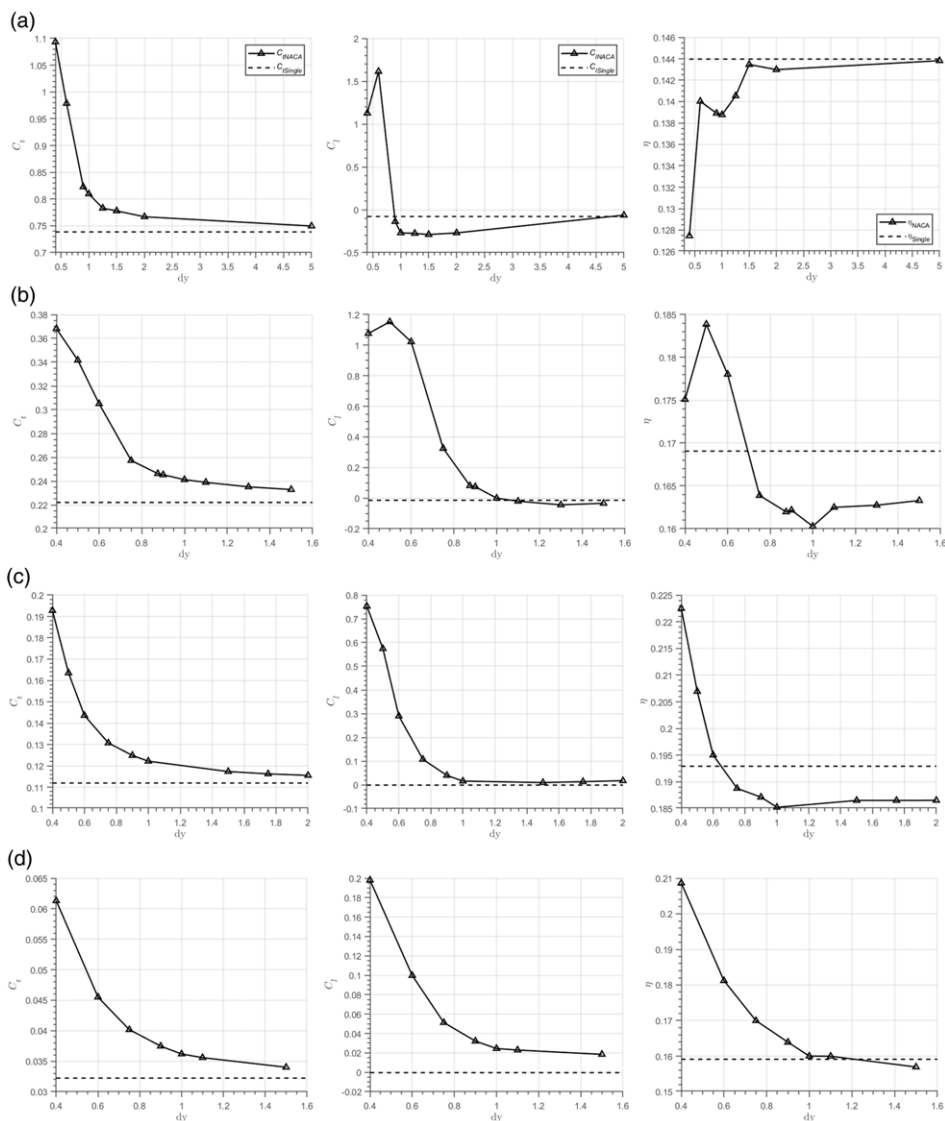


Figure 11. Variation of thrust coefficient, lift coefficient and propulsive efficiency for (a) $k = 12.7$, $v_p = 1.12$, $Re = 1,960$, (b) $k = 8.4$, $v_p = 0.74$, $Re = 2,990$, (c) $k = 6.3$, $v_p = 0.55$, $Re = 3,960$, and (d) $k = 4.2$, $v_p = 0.37$, $Re = 5,940$.

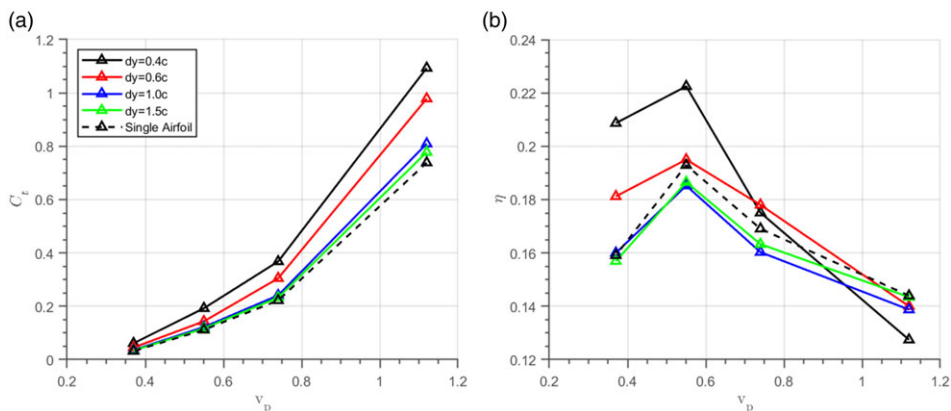


Figure 12. Variation of (a) the thrust coefficient and (b) propulsive efficiency with respect to nondimensional plunge velocity for different wall distances.

It is instructive to observe the change in vortex shedding as a function of wall distance and plunge velocity. Dohring [15] found it necessary to distinguish between wall distances $dy < 0.5c$, $0.5c < dy < 1.0c$, $dy > 1.0c$ and plunge velocities $v_p > 1$ and $v_p < 1$. It is well known that in unbounded flow the vortex shedding occurs in the form of a symmetric reverse Karman vortex street for $v_p < 1$ that becomes asymmetric for $v_p > 1$, deflected upwards or downwards depending on the initial starting motion of the foil. Dohring's flow visualisation revealed that for $dy < 0.5c$ and small v_p a row of clockwise vortices is shed along the plate and counterclockwise vortices are weak or not visible at all. For $v_p > 1$ a row of counterclockwise vortices is shed along the plate and the clockwise vortices are weak or invisible. Therefore, in the former case the induced velocities are negative and the maximum flow velocity cannot occur near the plate, whereas in the latter case the induced velocities are positive and the maximum velocity will always be close to the plate. For distances between $0.5c$ and $1.0c$, the ground effect changes the symmetric vortex shedding into an upward deflected shedding of vortex pairs. This change is visible in Fig. 13(a), (b), (c), (d) for wall distances $< 0.9c$. The deflection does not depend on the initial plunge direction. At wall distances $> 1.0c$, its effect has become minimal. This pairing phenomenon has also been observed for pure pitch oscillations in ground proximity by Quin et al. [25]. For low k and small wall distances, the vorticity is elevated away from the ground and pushed downstream by the counterclockwise vortex as shown in Fig. 14. This vorticity is denoted as ground vorticity by Molina et al. [26].

6.0 Application to flat plate boundary layer flow

The MAV, shown in Fig. 1, benefited greatly from the ground effect phenomenon by positioning two aerofoils flapping in counterphase in a biplane arrangement downstream of the fixed wing's trailing edge. In order to demonstrate the direct boundary layer propulsion method by oscillating foils proposed in the present paper, the flow over the flat plate configuration shown in Fig. 2(b) was computed. The two foils are again flapping in counterphase, but they are mounted upstream of the plate trailing edge.

Figure 15 shows the variation of the thrust produced by the upper aerofoil, lower aerofoil, the drag of the flat plate and the thrust of the complete configuration at the wall distances of $0.4c$ and $1.5c$ by adding the thrust of the two oscillating foils and subtracting the drag of the plate. The coefficients are nondimensionalised with the chord length of the aerofoils. For $k = 12.7$, the upper and lower aerofoils generate an almost identical thrust force. As expected, their values decrease from around 1.1 to 0.75 as the wall distance increases from $0.4c$ to $1.5c$. These values are very close to the results obtained in the previous section from the plunging aerofoil near the flat plate at a position far upstream from the plate trailing edge. However, a significant difference can be observed in Fig. 16 between oscillating the

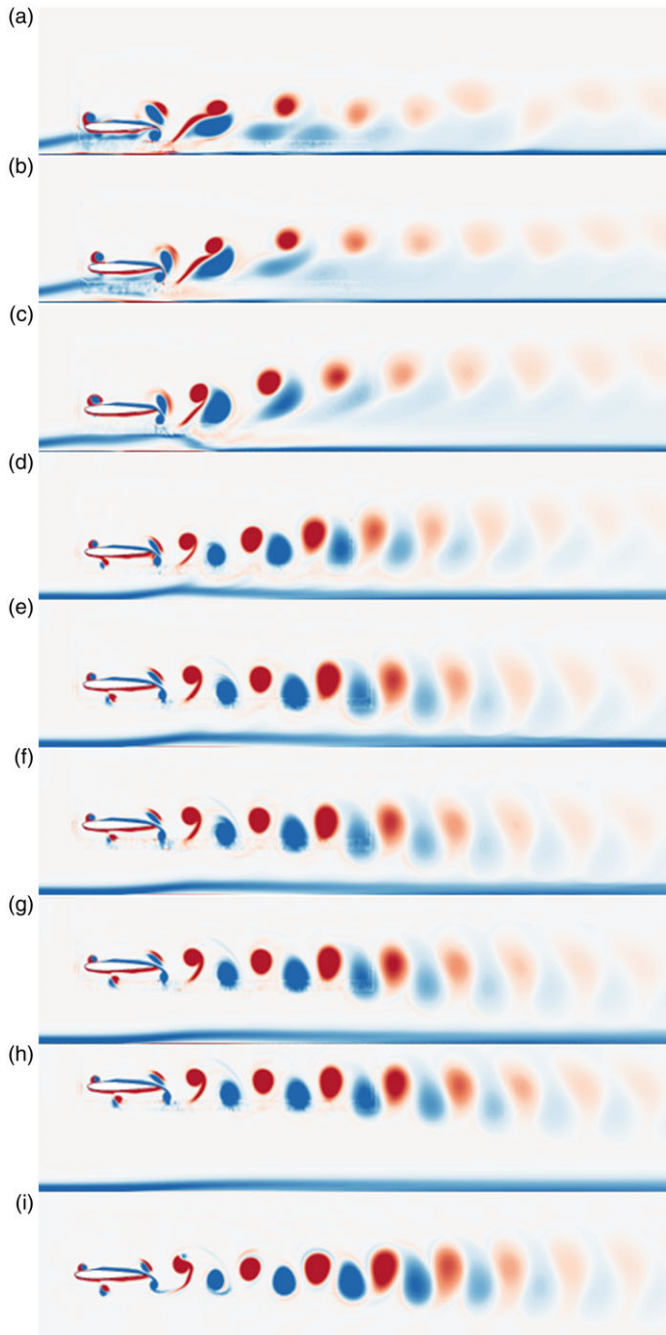


Figure 13. Instantaneous vorticity field for (a) $dy = 0.4c$, (b) $dy = 0.5c$, (c) $dy = 0.6c$, (d) $dy = 0.75c$, (e) $dy = 0.9c$, (f) $dy = 1.0c$, (g) $dy = 1.1c$, (h) $dy = 1.5c$, and (i) single plunging aerofoil at $k = 8.38$, $v_p = 0.74$, $Re = 2,990$.

foils in the boundary layer at $dy = 0.4c$ versus outside the boundary layer at $dy = 1.5c$. As expected, no interaction takes place between the Karman vortex street shed from the flat plate in the latter case. In the former case, the Karman vortex street is prevented from forming, resulting in an approximately 40% drag reduction of the flat plate.

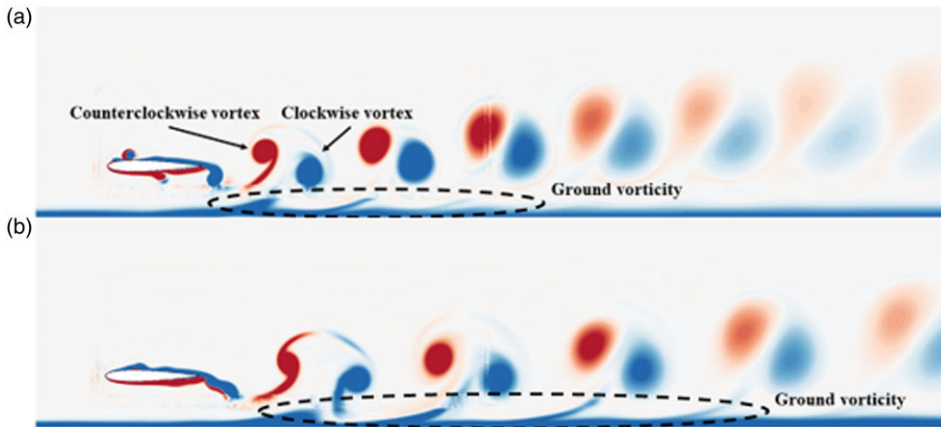


Figure 14. Instantaneous vorticity field for $dy = 0.6c$ at (a) $k = 6.3$, and (b) $k = 4.2$.

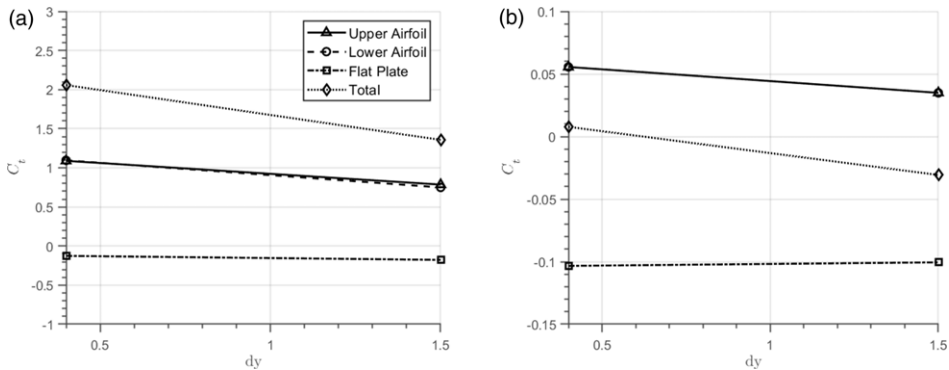


Figure 15. Influence of wall distance on the thrust produced by upper aerofoil, lower aerofoil, and flat plate at (a) $k = 12.7$, and (b) $k = 4.2$.

Similarly, as shown in Fig. 17, for the lower plunge frequency and higher Reynolds number case of $k = 4.2$ and $Re = 5,940$, there is no interaction between the Karman vortex street and the vortices shed from the aerofoils at a wall distance of $dy = 1.5c$, but a very strong interaction at $dy = 0.4c$. In the former case the thrust of the aerofoils is too small to overcome the plate drag while in the latter case it is still sufficient to produce a net thrust.

7.0 Summary and outlook

The flight speed of vehicles using flapping wing propulsion is limited because the required high Strouhal number can only be achieved by a low speed in the denominator of the Strouhal number. However, aerofoils or hydrofoils oscillating in a vehicle's boundary layer encounter low flow speeds while the vehicle's flight speed may be significantly larger. The investigation of oscillating foils in or close to vehicle boundary layers therefore may open possibilities for boundary layer energisation that deserve exploration.

The analysis presented in this paper shows that small foils oscillating in the pure plunge mode in or close to the boundary layer of a flat plate generate significantly larger thrust than foils oscillating in an unbounded flow of equal Reynolds number, thus indicating the possibility of favorably influencing the

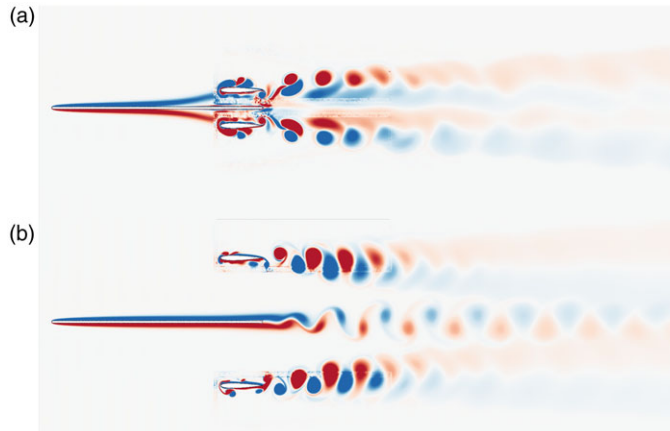


Figure 16. Instantaneous vorticity field for biplane arrangement for $k = 12.7$, $v_p = 1.12$, $Re = 1,960$ at (a) $dy = 0.4c$, and (b) $dy = 1.5c$.

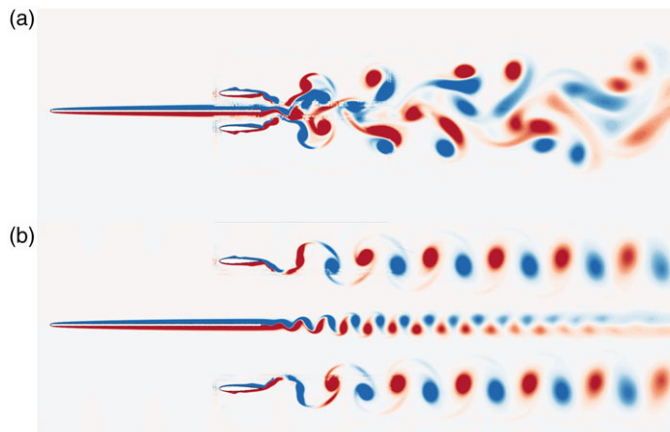


Figure 17. Instantaneous vorticity field for biplane arrangement for $k = 4.2$, $v_p = 0.37$, $Re = 5,940$ at (a) $dy = 0.4c$, and (b) $dy = 1.5c$.

boundary layer behaviour on large-scale aerofoils or hydrofoils. The results also show beneficial interaction effects between the Karman vortex street shed by the flat plate and the vortices shed by the flapping foils. Such foils therefore can be regarded as oscillating vortex generators (OVG) in generalisation of the well-known steady-state (VG) vortex generators.

References

- [1] Jones, K.D., Bradshaw, C.J., Papadopoulos, J. and Platzer, M.F. Bio-inspired design of flapping-wing micro air vehicles, *Aeronaut. J.*, 2005, **109**, (1098), pp 385–393.
- [2] Dohring, C.M., Fottner, L. and Platzer, M.F. Experimental and numerical investigations of flapping wing propulsion and its application for boundary layer control, ASME 1998 International Gas Turbine and Aeroengine Congress and Exhibition, 1998, GT-046.
- [3] Moryossef, Y. and Levy, Y. Effect of oscillations on airfoils in close proximity to the ground, *AIAA J.*, 2004, **42**, (9), pp 1755–1764.
- [4] Liang, H., Wang, X., Zou, L. and Zong, Z. Numerical study of two-dimensional heaving airfoils in ground effect, *J. Fluids Struct.*, 2014, **48**, pp 188–202.
- [5] Molina, J. and Zhang, X. Aerodynamics of a heaving airfoil in ground effect, *AIAA J.*, 2011, **49**, (6), pp 1168–1179.

- [6] Wu, J., Shu, C., Zhao, N. and Yan, W. Fluid dynamics of flapping insect wing in ground effect, *J. Bionic Eng.*, 2014, **11**, (1), pp 52–60.
- [7] Sarbandi, A., Naderi, A. and Parhizkar, H. The ground effect on flapping Bio and NACA 0015 airfoils in power extraction and propulsion regimes, *J. Braz. Soc. Mech. Sci. Eng.*, 2020, **42**, (287), pp 1–17.
- [8] Rozhdstvensky, K. Asymptotic theory of flapping wing propulsion in extreme ground effect, *Appl. Sci.*, 2023, **13**, (2), pp 690.
- [9] Knoller, R. Die Gesetze des Luftwiderstandes, *Flug- und Motortechnik*, 1909, **3**, (21), pp 1–7.
- [10] Betz, A. Ein Beitrag zur Erklärung des Segelfluges, *Zeitschrift für Flugtechnik and Motorluftschiffahrt*, 1912, **3**, pp 269–272.
- [11] Katzmayer, R. Effect of Periodic Changes of Angle of Attack on Behavior of Airfoils, NACA-T.M. 147, April 1922.
- [12] Shyy, W., Aono, H., Kang, C. and Liu, H. An Introduction to Flapping Wing Aerodynamics, Cambridge University Press, 2013, New York.
- [13] Platzer, M.F. Integrated propulsion/lift/control system for aircraft and ship applications, U.S. Patent Number 5,975,462, filed 2 Nov. 1999.
- [14] Lai, J.C.S., Yue, J. and Platzer, M.F. Control of backward facing step flow using a flapping airfoil, *Exp. Fluids*, 2002, **32**, pp 44–54.
- [15] Dohring, C.M. Der Schub des schlagenden Flügels und seine Anwendung zur Grenzschichtbeeinflussung: eine experimentelle und numerische Untersuchung, PhD Thesis, Armed Forces University Munich, Germany, 1998.
- [16] Anilir, B., Kurtulus, D.F. and Platzer, M.F. Flow control by oscillating trailing-edge flaps, *AIAA J.*, 2023, **61**, (9), pp 4210–4213.
- [17] ANSYS Inc. ANSYS Fluent User's Guide, Release 17.2, 2016.
- [18] Ferziger, J.H., Peric, M. and Street, R.L. *Computational Methods for Fluid Dynamics*, 4th ed, Springer, 2020, Switzerland.
- [19] Menter, F.R. Two-equation eddy-viscosity turbulence models for engineering applications, *AIAA J.*, 1994, **32**, (8), pp 1598–1605.
- [20] Langtry, R.B. and Menter, F.R. Correlation-based transition modeling for unstructured parallelized computational fluid dynamics codes, *AIAA J.*, 2009, **47**, (12), pp 2894–2906.
- [21] Counsil, J.N.N. and Boulama, K.G. Low-Reynolds-number aerodynamic performances of the NACA 0012 and Selig–Donovan 7003 airfoils, *J. Aircraft*, 2013, **50**, (1), pp 204–216.
- [22] Chen, F., Yu, J. and Mei, Y. Aerodynamic design optimization for low Reynolds tandem airfoil, *Proc. IMechE Part G: J. Aerospace Eng.*, 2018, **232**, (6), pp 1047–1062.
- [23] Ruiz, M.C. and D'Ambrosio, D. Validation of the γ - $Re\theta$ transition model for airfoils operating in the very low Reynolds number regime, *Flow, Turbul. Combust.*, 2022, **109**, pp 279–308.
- [24] Anilir, B., Kurtulus, D.F. and Platzer, M.F. Aerodynamics of close-coupled stationary/flapping tandem NACA 0012 airfoils, AIAA Aviation Forum, San Diego, CA, USA, June 2023.
- [25] Quinn, D.B., Moored, K.W., Dewey, P.A. and Smits, A.J. Unsteady propulsion near a solid boundary, *J. Fluid Mech.*, 2014, **742**, pp 152–170.
- [26] Molina, J., Zhang, X. and England, D. On the unsteady motion and stability of a heaving airfoil in ground effect, *Acta Mech. Sinica*, 2011, **27**, (2), pp 164–178.